Studies of coupled metallic magnetic thin-film trilayers

S. M. Rezende, C. Chesman, M. A. Lucena, A. Azevedo,
and F. M. de Aguiar[a)]
Departamento de Física, Universidade Federal de Pernambuco, 50670-901 Recife, PE, Brazil

S. S. P. Parkin
IBM Research Division, Almanden Research Center, 650 Harry Road, San Jose, California 95120-6099

(Received 5 January 1998; accepted for publication 24 March 1998)

Results are reported of a detailed study of static and dynamic responses in symmetric systems consisting of two ferromagnetic films separated by a nonferromagnetic spacer layer. A comparison is made with experimental results for two systems grown by sputter deposition in an UHV chamber, namely, NiFe/Cu/NiFe and Fe/Cr/Fe. First, we present model calculations where the coupling between the magnetic films through magnetic dipolar, bilinear, and biquadratic exchange interactions are fully taken into account, together with surface, in-plane uniaxial, and cubic anisotropies. An analytical expression is given that can readily be used to consistently interpret magnetoresistance, magneto-optical Kerr effect, ferromagnetic resonance, and Brillouin light scattering (BLS) data in such trilayers. Application of the results to BLS data in $Ni_{81}Fe_{19}(d)/Cu(25\ Å)Ni_{81}Fe_{19}(d)$, with $d=200$ and 300 Å, shows that it is essential to treat the dipolar interaction adequately in moderately thick systems. The results are also applied to interpret very interesting data in $Fe(40\ Å)/Cr(s)/Fe(40\ Å)$, with $5\ Å<s<35\ Å$, investigated by the four techniques mentioned above, at room temperature. It is shown that consistent values for all magnetic parameters can be extracted from the data with a theory that treats both static and dynamic responses on equal footing. © *1998 American Institute of Physics.* [S0021-8979(98)00913-X]

I. INTRODUCTION

Brillouin light scattering (BLS) and ferromagnetic resonance (FMR) are among the best experimental techniques to determine the interlayer exchange coupling between ferromagnetic films separated by a nonmagnetic metallic spacer. Measurement of this coupling as a function of spacer and magnetic layer thicknesses, temperature, interface properties, and various material parameters, are essential to test theories underlying the coupling mechanisms and to study basic properties of artificial structures. In addition to the interlayer coupling, the BLS and FMR data also provide unique information on the magnetic anisotropy and magnetization of the ferromagnetic layers.

In order to interpret the BLS and FMR data it is necessary to have knowledge of the spin-wave dispersion relations. The BLS spectra provide information on the volume and surface modes with nonzero wave vector, $q\neq 0$, whereas the FMR technique probes the surface modes in the uniform, $q=0$ limit.[1] The spin-wave mode configurations and dispersion relations are strongly dependent on the coupling between the magnetizations in the magnetic layers. This coupling arises from the dipolar stray fields and the exchange interaction. The dipolar coupling has been a familiar mechanism for several decades.[2–4] It dominates the interaction between the magnetic layers in relatively thick structures. With the advance in fabrication techniques, it has become possible to control the epitaxial growth layer by layer in atomic scale. Nearly ten years ago, it was then found that metallic spacers with a few atomic monolayers give rise to an effective exchange coupling,[5] described by an interaction energy bilinear in the magnetizations of the films.[6] This bilinear interaction is characterized by an exchange constant which can be positive or negative, corresponding to ferromagnetic or antiferromagnetic alignment of the neighboring magnetizations. More recently it was discovered that certain systems exhibit an additional exchange coupling, modeled by a biquadratic interaction energy,[7,8] that can make the two magnetizations align at 90° to each other.

The spin-wave dispersion relations for trilayer structures have been calculated by several authors. The earlier calculations,[3,4] made before the exchange coupling was discovered, considered only the effect of the dipolar interaction on the surface and volume magnetostatic modes in the coupled films. The simultaneous presence of dipolar and exchange interactions complicates the problem considerably. The equations of motion involve three components of the magnetization and the dipolar magnetic field in each layer, matched by the appropriate boundary conditions at the interfaces. The full solutions including the bilinear exchange coupling, but restricted to ferromagnetic alignment, were worked out by Hillebrands[9] for an arbitrary number of magnetic layers. For a trilayer structure, formed by two magnetic films separated by a nonmagnetic spacer, the dispersion relation is obtained from a system of 16 linear equations. This requires the use of appropriate numerical tools which complicate the interpretation of the observed spectra. This fact, added to the need to interpret data in systems with antiferromagnetic coupling, led several authors to develop alternative

[a)]Electronic mail: fma@df.ufpe.br

calculations, each with its own limitations or simplifying assumptions.[10–19]

In this paper we present a calculation of the spin-wave dispersions for a trilayer structure with bilinear and biquadratic coupling, which can readily be used to interpret BLS and FMR experiments. The calculation takes into account an applied static magnetic field in the film plane, surface and in-plane uniaxial and cubic crystalline anisotropies, and bilinear and biquadratic exchange interactions with arbitrary signs and magnitudes. The approach used is based on the equations of motion for the small-signal magnetization deviations from the equilibrium directions, similar to that of Cochran and co-workers.[12,16] However, besides introducing the biquadratic coupling, our calculation differs from Cochran's by an improved treatment of the dipolar interaction, which makes the results suitable for reasonably thick magnetic layers. The following section is devoted to energy considerations while the spin-wave dispersion relations are derived in Sec. III. Section IV describes details of the experimental techniques and sample preparation. In Sec. V the theoretical results are applied to interpret BLS and FMR experiments in NiFe/Cu/NiFe trilayers with moderately thick magnetic layers, for which the coupling is mainly due to the dipolar interaction. Section VI presents a unified picture of quite interesting magneto-optical Kerr effect (MOKE), MR, BLS, and FMR data in a series of sputtered single-crystal (100) Fe/Cr/Fe trilayers with varying Cr thickness. Finally, Sec. VII summarizes the main results.

II. ENERGY CONSIDERATIONS: STATIC PROPERTIES

The calculation presented here is based on the continuum approach used by Hillebrands, Cochran *et al.*, and other authors.[9–12] The geometry and the coordinate system employed are shown in Fig. 1. We consider two magnetic thin single-crystal films, 1 and 2, having cubic lattice structure. They have thicknesses d_1 and d_2 and are separated by a nonmagnetic spacer layer with thickness s. The coordinate system is chosen so that the xz plane is parallel to the film surface, with the x and z axes along [100] and [001] crystal directions, respectively. We study only the situation where the external static magnetic field $\mathbf{H}_0$ is applied in the plane of the films, at an arbitrary angle θ_H with respect to the [001] direction. In this case, the equilibrium directions of the magnetizations of the two films, $\mathbf{M}_1$ and $\mathbf{M}_2$, are also in the xz plane, characterized by the polar angles θ_1 and θ_2. As is well known, the static and dynamic responses result from the competition of several interactions. In general, each interaction tries to align the magnetizations of the two magnetic films along different directions. Since there is a close relationship between the static configuration and the dynamic response of the system, the frequencies of the magnetic excitations depend strongly on the equilibrium configuration of the magnetizations. Therefore our initial goal is to determine the equilibrium values of θ_1 and θ_2.

The equilibrium directions of $\mathbf{M}_1$ and $\mathbf{M}_2$ are determined by the minima of the total free energy. We consider a free energy per unit area with four basic contributions:

$$E = E_z + E_a + E_{\text{ex}} + E_{\text{dip}}, \tag{1}$$

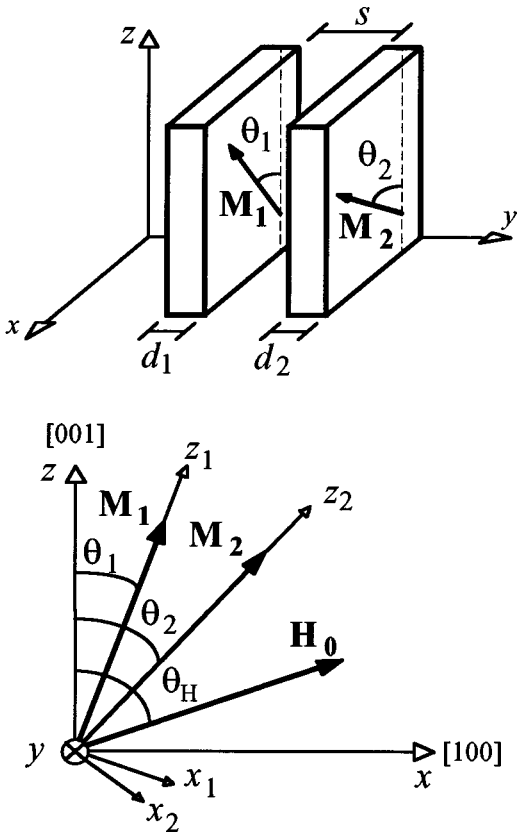

FIG. 1. Trilayer structure (upper panel) and coordinate systems (lower panel) used to represent the fields and magnetizations in the two magnetic layers. The axes z_1 and z_2 are chosen to coincide with the equilibrium directions of $\mathbf{M}_1$ and $\mathbf{M}_2$.

where the subscripts denote, in order, Zeeman, anisotropy, exchange, and dipolar terms. The Zeeman energy per unit area is

$$E_z = -\sum_{i=1}^{2} d_i \mathbf{M}_i \cdot \mathbf{H}_0 . \tag{2}$$

The anisotropy energy has three contributions: E_{ac} is the cubic magnetocrystalline energy; E_{au} is an in-plane uniaxial term due to distortions introduced by mismatches between the lattices of the films and the substrate; E_{as} is a surface energy due to the broken cubic symmetry at the film surfaces. These three contributions to the energy per unit area are

$$E_{\text{ac}} = \sum_i \frac{K_1^{(i)} d_i}{M_i^4} (M_{ix}^2 M_{iy}^2 + M_{ix}^2 M_{iz}^2 + M_{iy}^2 M_{iz}^2), \tag{3}$$

$$E_{\text{au}} = -\sum_i \frac{K_u^{(i)} d_i}{M_i^2} (\mathbf{M}_i \cdot \hat{\theta}_{ui})^2, \tag{4}$$

$$E_{\text{as}} = -\sum_i \frac{K_s^{(i)}}{M_i^2} M_{iy}^2, \tag{5}$$

where $K_1^{(i)}$ is the first-order cubic anisotropy constant of film i, $K_u^{(i)}$ is the uniaxial in-plane anisotropy constant in a direction defined by a polar angle $\theta_u^{(i)}$, $\hat{\theta}_u^{(i)}$ is the unit vector in that direction, and $K_s^{(i)}$ is the uniaxial surface anisotropy en-

ergy constant. Note that the anisotropy constants $K_1^{(i)}$ and $K_u^{(i)}$ have units of erg/cm^3 and each one is associated with an effective anisotropy field $H_a^{(i)}=2K^{(i)}/M_i$ with units of Oe. Usually the anisotropy parameters are the same for both magnetic films, so that the superscript (i) can be dropped for simplicity.

The exchange energy has the usual volume intralayer exchange contribution plus the interlayer exchange coupling, composed of bilinear $E_{\rm ex1}$ and biquadratic $E_{\rm ex2}$ terms, given by

$$E_{\rm ex1}=-J_1\,\frac{\mathbf{M}_1\cdot\mathbf{M}_2}{M_1M_2}, \tag{6}$$

$$E_{\rm ex2}=J_2\left(\frac{\mathbf{M}_1\cdot\mathbf{M}_2}{M_1M_2}\right)^2, \tag{7}$$

where J_1 and J_2 are the so-called bilinear and biquadratic coupling constants, which have units of erg/cm^2. They are associated to effective exchange fields $H_{\rm ex1}^{(i)}=J_1/M_id_i$ and $H_{\rm ex2}^{(i)}=J_2/M_id_i$ with units of Oe. Note that $J_1>0$ and $J_1<0$ correspond, respectively, to ferromagnetic and antiferromagnetic couplings. In the case of the biquadratic coupling, $J_2>0$ tends to make the magnetizations in the two films to lie at 90° to one another. As will be shown later, in some systems the biquadratic coupling is sufficiently large and dominates in the determination of the equilibrium configuration of the magnetizations, having a marked influence on the spin-wave frequencies.

Finally, the dipolar energy has surface and volume contributions. The surface contribution, also called demagnetizing energy, is given by

$$E_{\rm demag}=\sum_i\,2\pi d_iM_{iy}^2, \tag{8}$$

which has the same form as the surface anisotropy energy (5). The volume contribution is associated with the magnetic field created by the spatial variations of the small-signal magnetization. Since it contributes to the dynamics of the system but not to the equilibrium configuration, we leave its discussion for Sec. III.

If the external magnetic field is applied in the plane of the films and the combination of the surface anisotropy and demagnetizing effects has an easy-plane character, the two magnetizations are confined to the xz plane. In this case $M_{iy}=0$ so that the relevant energy per unit area to determine the equilibrium configuration is, from Eqs. (1)–(8):

$$E=\sum_{i=1}^{2}\,d_i\Big[-M_iH_0\,\cos(\theta_i-\theta_H)+\frac{1}{4}\,K_1^{(i)}\,\sin^2 2\theta_i - K_u^{(i)}\,\cos^2(\theta_i-\theta_u^{(i)})\Big]-J_1\,\cos(\theta_1-\theta_2) + J_2\,\cos^2(\theta_1-\theta_2). \tag{9}$$

In simple situations the equilibrium configuration can be obtained analytically by equating to zero the derivatives of the energy in Eq. (9) with respect to θ_1 and θ_2. However, in more general situations this leads to transcendental equations which cannot be solved analytically. In the cases studied in this paper, the equilibrium configuration was determined numerically by varying θ_1 and θ_2, first in steps of 5°, to locate the range of minimum energy, and then in steps of 0.5° to obtain accurate minima values.

Once θ_1 and θ_2 are found, we obtain normalized values for the magnetoresistance from

$$\frac{R(H_0)}{R(0)}=\frac{1-\cos(\theta_1-\theta_2)}{2}, \tag{10}$$

and for the magnetization component in the field direction from

$$\frac{M(H_0)}{M_S}=\frac{M_1\,\cos(\theta_1-\theta_H)+M_2\,\cos(\theta_2-\theta_H)}{M_1+M_2}. \tag{11}$$

In (10) $R(0)$ is the resistance in the absence of the external magnetic field, and in (11) M_s is the total saturation magnetization. These two equations will be used to fit MR and MOKE data, respectively, as presented in Sec. VI.

III. DERIVATION OF THE SPIN-WAVE DISPERSION

In this section we derive the spin-wave dispersion relations for the trilayer structure which are used to interpret the BLS and FMR data. The calculation is based on the torque equations of motion for the continuous magnetizations of the two magnetic films. Similar calculations have been made by several authors.[9–20] The novelty here is the introduction of the biquadratic exchange coupling and the use of an improved approximation for the dipolar coupling, which makes the results valid for relatively thick magnetic layers.

The equation of motion for the magnetization of film i is written as

$$\frac{d}{dt}\,\mathbf{M}_i=\gamma_i\mathbf{M}_i\times\mathbf{H}_{\rm eff}^{(i)}, \tag{12}$$

where $\gamma_i=g_i\mu_B/\hbar$ is the gyromagnetic ratio ($\gamma_i/2\pi=2.8$ GHz/kOe for $g_i=2$) and $\mathbf{H}_{\rm eff}^{(i)}$ is the effective field acting on $\mathbf{M}_i$. All fields and magnetizations are decomposed into a static part and a small-signal dynamic component.

For each film we use a Cartesian coordinate system $x_iy_iz_i$, obtained from the one with the axes in the [100] directions, by rotation about the y axis so that the z_i axis coincides with the equilibrium direction of the magnetization $\mathbf{M}_i$, as shown in the lower panel of Fig. 1. Hence, the magnetization in film i can be written as

$$\mathbf{M}_i=\hat{x}_im_{ix_i}+\hat{y}_im_{iy}+\hat{z}_iM_{iz_i}, \tag{13}$$

where it is assumed that m_{ix_i}, $m_{iy}\ll M_{iz_i}$. The transformation from the original variables is given by

$$M_{ix}=M_{iz_i}\,\sin\,\theta_i+m_{ix_i}\,\cos\,\theta_i, \tag{14}$$

$$M_{iy}=m_{iy}, \tag{15}$$

$$M_{iz}=M_{iz_i}\,\cos\,\theta_i-m_{ix_i}\,\sin\,\theta_i. \tag{16}$$

Likewise, the effective field is written as

$$\mathbf{H}_{\rm eff}^{(i)}=\hat{x}_ih_{ix_i}+\hat{y}h_{iy}+\hat{z}_iH_{iz_i}. \tag{17}$$

The effective fields corresponding to the Zeeman, anisotropy, bilinear, and biquadratic exchange energy contributions E_λ are given by

$$\mathbf{H}_\lambda^{(i)} = -\nabla_{M_i}(E_\lambda / d_i). \tag{18}$$

The calculation of the volume dipolar magnetic field is more involved and requires some approximations in order to be carried out analytically, as will be shown later. Since the spin-wave frequencies are determined by the linearized equations, in the transformation of the energy expressions (2)–(9) to the new variables (13) and (17), only terms quadratic in small-signal components have to be kept. Furthermore, in the calculation of the effective fields, only terms linear in small quantities in the x_i and y_i components and constant in the z_i components need to be retained. Note also that it is not necessary to expand the M_{iz_i} components into m_{ix_i}, and m_{iy_i}, as prescribed in Ref. 12. It is simpler to evaluate the derivatives of E_λ with respect to M_{iz_i} and enter the equation of motion with the corresponding z_i components of the effective fields.

From the Zeeman energy we obtain only one relevant field component,

$$H_{iz_i}^z = -\frac{1}{d_i}\frac{\partial E_z}{M_{iz_i}} = H_0 \cos(\theta_i - \theta_H). \tag{19}$$

The contributions from the cubic anisotropy energy to the effective field are

$$h_{ix_i}^{\mathrm{ac}} \simeq \frac{K_1^{(i)}}{M_i^2} m_{ix_i}(3\sin^2 2\theta_i - 2), \tag{20}$$

$$h_{iy}^{\mathrm{ac}} \simeq -\frac{2K_1^{(i)}}{M_i^2} m_{iy}, \tag{21}$$

$$H_{iz_i}^{\mathrm{ac}} \simeq -\frac{K_1^{(i)}}{M_i} \sin^2 2\theta_i. \tag{22}$$

The relevant components of the uniaxial anisotropy field are

$$h_{ix_i}^{\mathrm{au}} \simeq \frac{2K_u^{(i)}}{M_i^2} \sin^2(\theta_i - \theta_u^{(i)}) m_{ix_i}, \tag{23}$$

$$H_{iz_i}^{\mathrm{au}} \simeq \frac{2K_u^{(i)}}{M_i} \cos^2(\theta_i - \theta_u^{(i)}), \tag{24}$$

and from the surface anisotropy energy, the only component is

$$h_{iy}^{\mathrm{as}} = \frac{2K_s^{(i)}}{d_i M_i^2} m_{iy}. \tag{25}$$

Finally, from the bilinear and biquadratic exchange energies we obtain the following components:

$$h_{ix_i}^{\mathrm{ex}} \simeq \frac{J_1}{d_i M_1 M_2} m_{jx_j} \cos(\theta_1 - \theta_2) - \frac{2J_2}{d_i M_1 M_2} m_{jx_j} \cos[2(\theta_1 - \theta_2)] - \frac{2J_2}{d_i M_i^2} m_{ix_i} \sin^2(\theta_1 - \theta_2), \tag{26}$$

$$h_{iy}^{\mathrm{ex}} \simeq \frac{J_1}{d_i M_1 M_2} m_{jy} - \frac{2J_2}{d_i M_1 M_2} m_{jy} \cos(\theta_1 - \theta_2), \tag{27}$$

$$H_{iz_i}^{\mathrm{ex}} \simeq \frac{J_1}{d_i M_i} \cos(\theta_1 - \theta_2) - \frac{2J_2}{d_i M_i} \cos^2(\theta_1 - \theta_2). \tag{28}$$

The treatment of the dipolar magnetic field is far more involved and requires several approximations to be carried out analytically. This field does not exist when the magnetization is uniform and lies in the film plane therefore it was not considered in the calculation of the equilibrium configuration. However, when the magnetization deviates from equilibrium, its spatial variation creates uncompensated magnetic dipoles which in turn generate a magnetic field **h** that obeys Maxwell's equations. This field can be calculated using the magnetostatic approximation, $\nabla \times \mathbf{h} = 0$, and defining a magnetic potential Φ through $\mathbf{h} = -\nabla\Phi$. This potential satisfies a Poisson equation:

$$\nabla^2 \Phi = 4\pi \nabla \cdot \mathbf{M}, \tag{29}$$

and can be obtained by standard boundary value problems methods, thus providing both surface and volume contributions to the dipolar field. Grünberg[3] has worked out the problem for two parallel magnetic films with the full boundary conditions from Maxwell's equations but without other interactions. The dipolar field couples the excitations in the two films, giving rise to in-phase and out-of-phase surface magnon modes, also called, respectively, acoustic and optic modes, propagating perpendicularly to the applied field. However, the presence of the exchange interaction between the films complicates the problem considerably. In order to treat the dipolar interaction in the same context as the other fields we follow the approach of Cochran *et al.*[12] in considering the field produced by one film and neglecting the effect of the boundary conditions on the second film. Assume a single semi-infinite film of thickness d with surfaces in the xz plane located at $y = \pm d/2$ with the static field applied along the z direction. Consider also that a magnetostatic surface wave propagates in the x direction, so that the deviation of the magnetization from equilibrium is given by

$$M_x(x) = M_x e^{iqx}, \quad M_y(x) = M_y e^{iqx}. \tag{30}$$

Solution of Eq. (29) with Eq. (30) yields the following dipolar field components in the three regions of interest.[12]

(i) Inside the film

$$h_x = [2\pi M_x e^{-qd/2}(e^{qy} + e^{-qy}) - 4\pi M_x - 2\pi i M_y e^{-qd/2}(e^{qy} - e^{-qy})] e^{iqx}, \tag{31}$$

$$h_y = [-2\pi i M_x e^{-qd/2}(e^{qy} - e^{-qy}) - 2\pi M_y e^{-qd/2}(e^{qy} + e^{-qy})] e^{iqx}. \tag{32}$$

(ii) To the right of the film ($y \geqslant d/2$)

$$h_x = 2\pi(M_x + iM_y)(e^{-qd/2} - e^{qd/2})e^{(-qy+iqx)}, \tag{33}$$

$$h_y = 2\pi(iM_x - M_y)(e^{-qd/2} - e^{qd/2})e^{(-qy+iqx)}. \tag{34}$$

(iii) To the left of the film ($y \leqslant -d/2$)

$$h_x = 2\pi(M_x - iM_y)(e^{-qd/2} - e^{qd/2})e^{(qy+iqx)}, \tag{35}$$

$$h_y = -\pi(iM_x - M_y)(e^{-qd/2} - e^{qd/2})e^{(-qy+iqx)}. \tag{36}$$

Clearly the nature of the dipolar field introduces a spatial variation with y that complicates the problem and requires further approximations. Cochran *et al.*[12] expand the exponential functions in the small parameters qy and qd to first order, simplifying the equations considerably. It turns out that in situations of interest this approximation is not satisfactory. Here we assume that the small-signal magnetizations do not vary along y and replace the dipolar fields by suitable averages[17] along y:

$$\langle \mathbf{h}_1^{\mathrm{dip}} \rangle = \frac{1}{d_1} \int_{-d_1/2}^{d_1/2} \mathbf{h}^{\mathrm{dip}}(y)\, dy, \tag{37}$$

$$\langle \mathbf{h}_2^{\mathrm{dip}} \rangle = \frac{1}{d_2} \int_{d_1/2+s}^{d_1/2+s+d_2} \mathbf{h}^{\mathrm{dip}}(y)\, dy. \tag{38}$$

Integration of Eqs. (31)–(36) yields the average dipolar field in film 1, for arbitrary direction of the applied in-plane field H:

$$\begin{aligned} \langle h_{1x}^{\mathrm{dip}} \rangle = & -4\pi M_{1x}[1 - (1 - e^{-qd_1})/qd_1] \\ & + 2\pi(iM_{2y} - M_{2x})(1 - e^{-qd_1}) \\ & \times [(1 - e^{-qd_2})e^{-qs}/qd_1]\cos(\theta_1 - \theta_H) \end{aligned} \tag{39}$$

$$\begin{aligned} \langle h_{1y}^{\mathrm{dip}} \rangle = & -4\pi M_{1y}(1 - e^{-qd_1})/qd_1 + 2\pi(iM_{2x} + M_{2y}) \\ & \times (1 - e^{-qd_1})(1 - e^{-qd_2})e^{-qs}/qd_1. \end{aligned} \tag{40}$$

The final expressions are obtained by introducing the transformation (14)–(16) in (39) and (40) and expanding the exponential functions in the parameters $qd_i \ll 1$. Similar expressions follow for the dipolar field in film 2. Using the resulting dipolar fields and the other field components (19)–(28) in Eq. (12), we obtain the appropriate equations of motion for the small-signal magnetizations in the two films. Assuming the time variation $\exp(i\omega t)$, where ω is the angular frequency, and retaining only terms to first order in small quantities we obtain

$$\begin{bmatrix} -i\omega/\gamma_1 & H_1 & iH_5 & H_2 \\ -H_3 & -i\omega/\gamma_1 & H_4 & iH_6 \\ -iG_5 & G_2 & -i\omega/\gamma_2 & G_1 \\ G_4 & -iG_6 & -G_3 & -i\omega/\gamma_2 \end{bmatrix} \begin{bmatrix} m_{1x_1} \\ m_{1y} \\ m_{2x_2} \\ m_{2y} \end{bmatrix} = 0, \tag{41}$$

where

$$\begin{aligned} H_1 = & H_0 \cos(\theta_1 - \theta_H) + \frac{H_{\mathrm{ac}}^{(1)}}{4}(3 + \cos 4\theta_1) + H_{\mathrm{au}}^{(1)} \cos^2(\theta_1 \\ & - \theta_u^{(1)}) - H_{\mathrm{as}}^{(1)} + 4\pi M_1(1 - qd_1/2) + D^{(1)}q^2 \\ & + H_{\mathrm{ex1}}^{(1)} \cos(\theta_1 - \theta_2) \\ & - 2H_{\mathrm{ex2}}^{(1)} \cos^2(\theta_1 - \theta_2), \end{aligned} \tag{42}$$

$$\begin{aligned} H_2 = & -H_{\mathrm{ex1}}^{(2)} - 2\pi M_1 qd_1(1 - qd_2/2)e^{-qs} + 2H_{\mathrm{ex2}}^{(2)} \cos(\theta_1 \\ & - \theta_2), \end{aligned} \tag{43}$$

$$\begin{aligned} H_3 = & H_0 \cos(\theta_1 - \theta_H) + H_{\mathrm{ac}}^{(1)} \cos 4\theta_1 \\ & + H_{\mathrm{au}}^{(1)} \cos[2(\theta_1 - \theta_u^{(1)})] \\ & + 2\pi M_1 qd_1 \cos^2(\theta_1 - \theta_H) + D^{(1)}q^2 \\ & + H_{\mathrm{ex1}}^{(1)} \cos(\theta_1 - \theta_2) - 2H_{\mathrm{ex2}}^{(1)} \cos[2(\theta_1 - \theta_2)], \end{aligned} \tag{44}$$

$$\begin{aligned} H_4 = & H_{\mathrm{ex1}}^{(2)} \cos(\theta_1 - \theta_2) - 2\pi M_1 qd_1(1 - qd_2/2)e^{-qs} \\ & \times \cos(\theta_1 - \theta_H)\cos(\theta_2 - \theta_H) - 2H_{\mathrm{ex2}}^{(2)} \cos[2(\theta_1 - \theta_2)], \end{aligned} \tag{45}$$

$$H_5 = \mp 2\pi M_1 qd_1(1 - qd_2/2)e^{-qs} \cos(\theta_2 - \theta_H), \tag{46}$$

$$H_6 = \pm 2\pi M_1 qd_1(1 - qd_2/2)e^{-qs} \cos(\theta_1 - \theta_H), \tag{47}$$

and G_1–G_6 are given by the same expressions as H_1–H_6 with $1 \leftrightarrow 2$. Note that $D^{(i)}$ is the intralayer exchange stiffness constant for film i, which was introduced in the usual manner.[9,17] The upper and lower signs in Eqs. (46) and (47) correspond to the Stokes and anti-Stokes frequency shifts, respectively. As is well known[1,17,19] these are equal in the ferromagnetic phase but are somewhat different in the antiferromagnetic and spin-canted phases. Note that, besides the generalization for arbitrary field direction and inclusion of biquadratic exchange, expressions (41)–(47) differ from those in Ref. 12 in the dependence on the parameters qd_i and qs, and are identical only in the limit of vanishing qd_i and qs. As a result, our treatment provides a better approximation for the dipolar field, and, as will be shown in Sec. V, is applicable to film thicknesses of several hundred angstroms.

The solutions of Eq. (41) are found by requiring that the secular determinant vanishes. This leads to magnetic excitation frequencies which are given by the zeroes of the following:

$$\frac{\omega^4}{\gamma_1^2\gamma_2^2} + a\omega^2 + b\omega + c = 0, \tag{48}$$

where

$$\begin{aligned} a = & (G_2H_4 + G_4H_2 + G_5H_5 + G_6H_6)/\gamma_1\gamma_2 - H_1H_3/\gamma_2^2 \\ & - G_1G_3/\gamma_1^2, \end{aligned} \tag{49}$$

$$\begin{aligned} b = & (G_3G_5H_2 + G_1G_4H_5 - G_1G_6H_4 - G_2G_3H_6)/\gamma_1 \\ & + (G_6H_2H_3 + G_4H_1H_6 - G_5H_1H_4 - G_2H_3H_5)/\gamma_2, \end{aligned} \tag{50}$$

and

$$c = G_1G_6H_3H_5 + G_1G_3H_1H_3 + G_5G_6H_5H_6 + G_5G_6H_2H_4 + G_3G_5H_1H_6 + G_2G_4H_2H_4 - G_2G_3H_2H_3 - G_1G_4H_1H_4 + G_2G_4H_5H_6. \quad (51)$$

For any given applied field, Eq. (48) has two real solutions, corresponding to the acoustic and optic modes. Evidently, in order to find the frequencies one must first determine the equilibrium angle, as indicated previously. Note that the FMR technique probes the $q=0$ modes and since they are not influenced by the dipolar coupling the calculation simplifies considerably. In this case $H_5=H_6=G_5=G_6=0$ so that the term linear in ω in Eq. (48) vanishes. This allows the FMR frequencies to be determined analytically. For $\gamma_1=\gamma_2=\gamma$, we have

$$\left(\frac{\omega}{\gamma}\right)^2_{\pm} = -(a_0/2) \pm \sqrt{(a_0/2)^2 - c_0}, \quad (52)$$

where

$$a_0 = (G_2H_4 + G_4H_2 - H_1H_3 - G_1G_3)_{q=0},$$

$$c_0 = (G_1G_3H_1H_3 + G_2G_4H_2H_4 - G_2G_3H_2H_3 - G_1G_4H_1H_4)_{q=0}.$$

Let us apply the result (52) to the simple case of a trilayer having two identical magnetic films, coupled through a bilinear antiferromagnetic exchange. Consider further, that the in-plane anisotropy is uniaxial with easy axis in the z direction and that the external field H_0 is applied in this direction. In this case there are three equilibrium phases depending on the field value, as determined by minimizing (9) with vanishing θ_H, θ_u, K_1, and J_2. For increasing field, the first phase is in the range $0 \leqslant H_0 \leqslant \sqrt{H_u(2H_{ex}+H_u)} \equiv H_{SF}$, where H_{ex} is the absolute value of the antiferromagnetic bilinear exchange field and H_u is the uniaxial anisotropy field for both films. In this phase the magnetizations are aligned antiferromagnetically, i.e., $\theta_1=0$ and $\theta_2=180°$, and the FMR frequencies for the optic and acoustic modes obtained from (52) are

$$\left(\frac{\omega}{\gamma}\right)^2_{\pm} = H_0^2 - H_u^2 + (H_u+H_{ex})(2H_u+4\pi M_{eff}) \pm [H_0^2(2H_u+4\pi M_{eff})(2H_u+4\pi M_{eff}+4H_{ex}) + H_{ex}^2(4\pi M_{eff})^2]^{1/2}, \quad (53)$$

where $4\pi M_{eff}=4\pi M_s - H_{as}$. This result is identical to that obtained previously by Wigen *et al.*[15] As the field is increased beyond the spin–flop critical value H_{SF}, the magnetizations become canted with angles $\theta_1=\theta$ and $\theta_2=\pi-\theta$, where $\sin\theta=[H_0/(2H_{ex}-H_u)]$. As the field increases in the spin–flop phase the magnetizations rotate towards the z axis and the FMR frequencies vary with field as

$$\left(\frac{\omega}{\gamma}\right)^2_{\pm} = [2H_{ex}^2 + H_u(H_{ex}+4\pi M_{eff})]\sin^2\theta + (H_{ex} + 4\pi M_{eff})(H_{ex}-H_u) - H_{ex}^2 \pm H_{ex} \times [(2H_{ex}+8\pi M_{eff}+H_u)\sin^2\theta - (H_u+4\pi M_{eff})]. \quad (54)$$

Finally, when the field is increased beyond the critical value $H_c=2H_{ex}-H_u$, the magnetizations become aligned in the z direction. In this saturated, or ferromagnetic, phase, the FMR frequencies are

$$\left(\frac{\omega}{\gamma}\right)^2_{+} = (H_0+H_u)(H_0+H_u+4\pi M_{eff}), \quad (55)$$

$$\left(\frac{\omega}{\gamma}\right)^2_{-} = (H_0+H_u-2H_{ex})(H_0+H_u-2H_{ex}+4\pi M_{eff}), \quad (56)$$

which are, again, in agreement with Ref. 15. This result shows that the difference between the fields for resonance of the acoustic and optic modes in the ferromagnetic phase, observed at fixed frequency, yields a direct measurement of the exchange coupling field. In the case of the BLS technique the field is fixed and one observes the frequency shifts of the two modes. One difficulty encountered in both FMR and BLS is that the optic mode intensity is much smaller than that of the acoustic mode. In fact, as is well known,[1,14] for films of identical materials the intensity of the optic mode in the ferromagnetic phase is theoretically zero. Fortunately, experimental films are always somewhat different from each other and present various magnetic phases, so that although the optic mode is weak it can be observed in many situations.

IV. EXPERIMENTAL DETAILS AND SAMPLES

A. Techniques

The experiments were carried out with three standard techniques, namely magneto-optic Kerr effect magnetometry (MOKE), Brillouin light scattering spectroscopy (BLS), and ferromagnetic resonance (FMR). Some samples were also investigated by magnetoresistance (MR) measurements. All samples studied are made of single crystal films as determined by X-ray diffractometry.

The MOKE setup employs a He–Ne laser modulated in amplitude at 50 kHz by an elasto-optic modulator placed between crossed polarizers. Magnetic hysteresis loops were measured in the longitudinal Kerr effect configuration, with the light polarized along the dc magnetic field in the film plane.

The BLS measurements were carried out in the backscattering geometry,[1,19,20] using a Sandercock model tandem Fabry–Perot interferometer with active stabilization in a (2×3)-pass configuration. The light source was a single-mode stabilized argon ion laser operating at 5145 Å, with incident power in the range 60–100 mW. Light detection was made by photon counting using a cooled EG&G photodetector with 40% quantum efficiency and an average dark noise of 1.5 cps. The spectra were stored in 256 channels, each with a

gate length of 1 ms. Several hundred to a few thousand interferometer scans were used to record the spectra, depending on the signal intensity. All measurements were done at room temperature with the sample between the poles of an electromagnet, with the field in the film plane and perpendicular to the incidence plane of the light beam. The sample was mounted on a goniometer to allow for two independent rotations: rotation around the normal as to vary the field direction in the film plane; rotation around the field direction to vary the incident angle α and thus the spin-wave wave number $q=2k_L \sin\alpha$. Magnons with wave numbers in the range $0.4\times10^5\ \mathrm{cm}^{-1}<q<2.1\times10^5\ \mathrm{cm}^{-1}$ could then be probed in a magnetic field varying from 0 to 6 kOe.

The FMR measurements were carried out with a homemade microwave spectrometer employing a sweep oscillator with frequency stabilized at the cavity resonance. The spectra were obtained by sweeping the field at fixed frequency and monitoring the derivative of the absorption lines provided by field modulation at 1 kHz with Helmholtz coils mounted on the cavity walls. In order to change the frequency several retangular cavities were constructed to operate in the TE_{102} mode in the X and K microwave bands. All measurements were made at room temperature with the field applied in the film plane. In order to investigate the in-plane magnetic anisotropy the sample is rotated about the normal to its plane, maintaining the field in the plane.

B. Samples

All studies reported in this paper were carried out with single-crystal samples prepared at the IBM Almanden Research Center. Two sets of trilayer samples were studied: $Ni_{81}Fe_{19}(d)$/Cu(25 Å)/$Ni_{81}Fe_{19}(d)$ and Fe(40 Å)/Cr(s)/Fe(40 Å). The films were grown by magnetron sputter deposition in an ultrahigh vacuum chamber equipped with six 2-in. dc magnetron sputtering sources. The base pressure prior to deposition was typically 2×10^{-9} Torr and the sputter pressure was usually 3×10^{-3} Torr Ar.

The NiFe, or permalloy (Py), films have relatively large thicknesses, $d=200$ and 300 Å, and provide an excellent room for testing the spin-wave dispersion calculated with various approximations for the dipolar field. The Py/Cu/Py trilayers were deposited onto polished, chemically cleaned single-crystal (100) MgO, (110) MgO, and (0001) sapphire substrates, coated with Fe(5 Å)/Pt(5 Å)/Cu(50 Å) buffer layers. Symmetry and protection of the top Py layer were provided by a 50 Å thick Cu overcoat layer. The thicknesses were primarily determined from the deposition time for each layer. The deposition rates ($\sim$2 Å/s) were determined from the measured thicknesses of thick ($\sim$1000 Å) calibration films grown along with multilayers. The values of the layer thicknesses determined by this method were cross checked by x-ray reflectivity on selected samples.

The Fe/Cr/Fe trilayers were grown on MgO (100) substrates. Initially a Cr seed layer, at least 100 Å thick, was deposited on the substrate at temperatures ranging up to 525 °C in order to establish epitaxy. The subsequent Fe/Cr/Fe layers were deposited at 150–180 °C and were capped with a thin Cr layer. As previously reported,[21,22] the Fe/Cr/Fe samples grow on the (100) plane with the Fe [100] along the MgO [110] direction. All samples have the same Fe layer thickness, $d=40$ Å. Initial characterization of the coupling was made with a Cr wedged sample, with $0<s<70$ Å. Then several samples were prepared with uniform Cr thickness varying from 5 to 35 Å, a range that corresponds to the first two antiferromagnetic peaks. The (100) Fe/Cr/Fe samples are used here to study the effect of the biquadratic coupling on the equilibrium configuration and on the spin-wave dispersion.

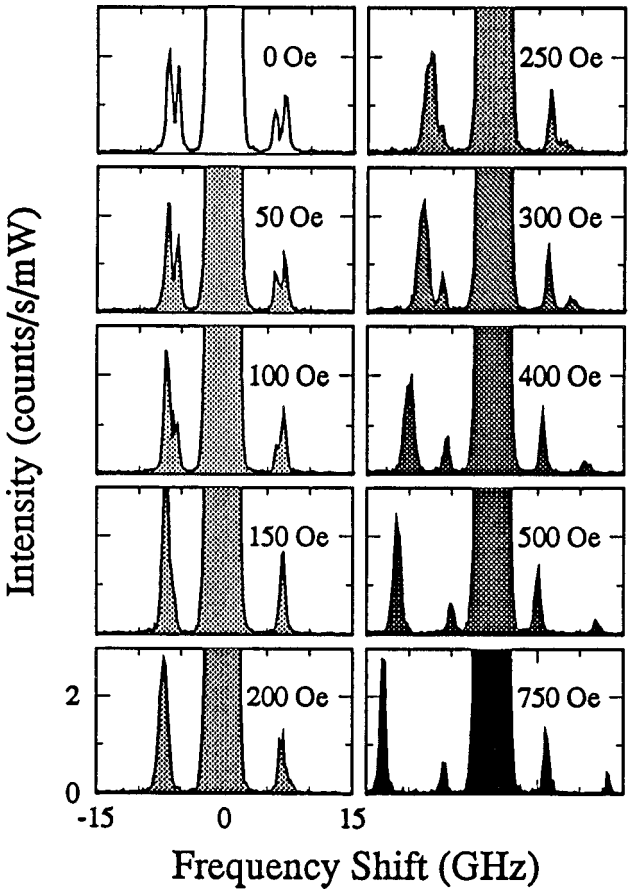

FIG. 2. BLS spectra for several values of the external field H_0 applied along a hard magnetization axis, observed in $Ni_{81}Fe_{19}$(200 Å)/Cu(25 Å)/$Ni_{81}Fe_{19}$(200 Å) grown onto (110)MgO. The grey scale indicates the magnetic field increase.

V. APPLICATION TO MODERATELY THICK FILMS: SPUTTERED Py/Cu/Py TRILAYERS

In this section we present BLS data only on (100) and (110) trilayers of Py(d)/Cu(25 Å)/Py(d) with $d=200$ and 300 Å, compare with the spin-wave theory developed in Sec. III, and demonstrate the reliability of the approximations made in the calculation of the dipolar field. This is possible because with a Cu spacer layer 25 Å thick the two Py films have negligible exchange interaction and then the nature of the coupled modes relies on the dipolar interaction.[10]

The BLS data, as well as the FMR, reveal that while the (100) samples are isotropic in the plane, as expected from the small cubic magnetocrystalline anisotropy of Py ($H_{ac}<5$ Oe), the (110) samples develop a strong uniaxial in-

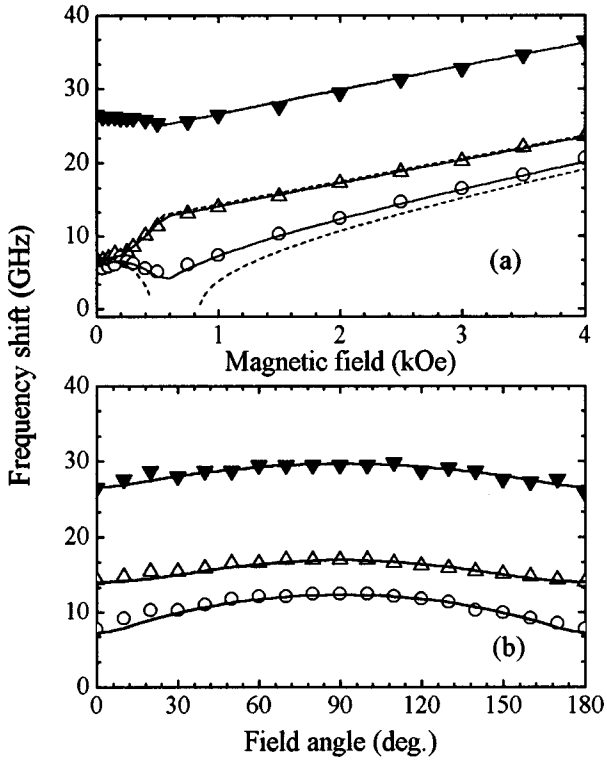

FIG. 3. Magnon frequencies for $q=1.73\times10^5$ cm^{-1} vs external field H_0, applied along the (a) hard magnetization axis ($\phi=0$) in $Ni_{81}Fe_{19}$(200 Å)/Cu(25 Å)/$Ni_{81}Fe_{19}$(200 Å) grown onto (110)MgO. Symbols are the BLS data: solid triangles for the lowest-order volume mode, open circles for the surface optic mode, and open triangles for the surface acoustic mode. Lines are results of calculations with Eq. (48) (solid), and theory in Ref. 12 (dashed). (b) Frequency shift for the same magnon wave number and $H_0=1$ kOe as a function of the in-plane field angle ϕ with respect to the hard axis.

plane anisotropy.[23] Figure 2 shows representative spectra in the low-field low-frequency region for the sample with $d=200$ Å grown on MgO (110), with the field applied parallel to a hard magnetization axis. All spectra were obtained with 500 scans, with laser power 80 mW at an angle of incidence of 45° corresponding to a scattering in-plane magnon wave number of 1.73×10^5 cm^{-1}. The spectra display intense acoustic and optic surface modes, with equal Stokes and anti-Stokes shifts. These modes have an apparently intriguing behavior with increasing field. The two inelastic scattering peaks first approach each other for $0<H_0<200$ Oe, then they split with increasing field. This separation reaches a maximum at about 750 Oe and decreases monotonically as the frequencies of both modes increase at higher field values. Not shown in Fig. 2 is the volume mode line about 26 GHz apart from the laser line, well outside the free spectral range. The behavior above is not observed when the field is applied parallel to an easy magnetization axis and, as discussed later, is due to a large uniaxial anisotropy characteristic of the samples grown on MgO (110). The measurements of the frequency shift versus magnetic field are shown by the symbols in the upper panel of Fig. 3. The calculated dispersion relations represented by the lines will be discussed later. The lower panel in Fig. 3 shows the frequency shifts as the sample is rotated around the normal to the film plane, in a

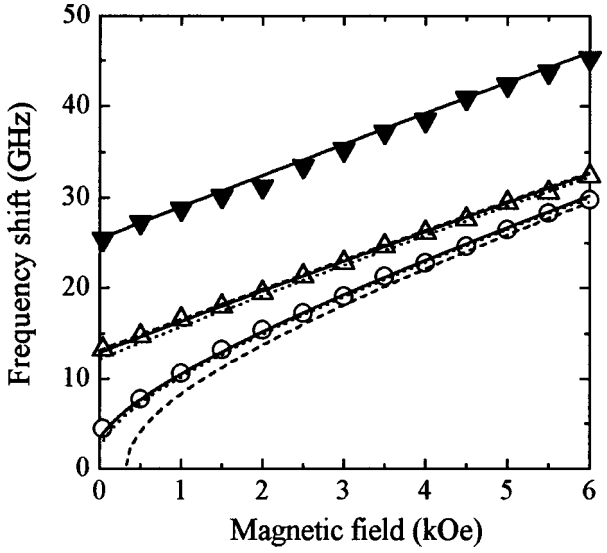

FIG. 4. The same as Fig. 3(a) in isotropic (100) $Ni_{81}Fe_{19}$(200 Å)/Cu(25 Å)/$Ni_{81}Fe_{19}$(200 Å). Lines are results of calculations with Eq. (48) (solid), theory in Ref. 12 (dashed), and theory in Ref. 3 (dotted).

magnetic field of 1 kOe. For simplicity, the in-plane field angle ϕ is defined here with respect to the hard magnetization axis. In contrast to the flat isotropic behavior observed in MgO (100) films, the samples grown on MgO (110) exhibit a twofold symmetric response, with a maximum at $\phi=90°$, where the field is applied parallel to an easy magnetization direction. The results above were confirmed by room-temperature angle-dependent FMR experiments. The source of the uniaxial in-plane anisotropy is probably the stress induced by lattice mismatch.[21]

Similar spectra were observed in the samples grown on MgO (110) with the field applied along an easy magnetization axis and in the samples grown on MgO (100). However, in these cases all frequencies increase monotonically with increasing field. This is seen in the dispersion relations mea-

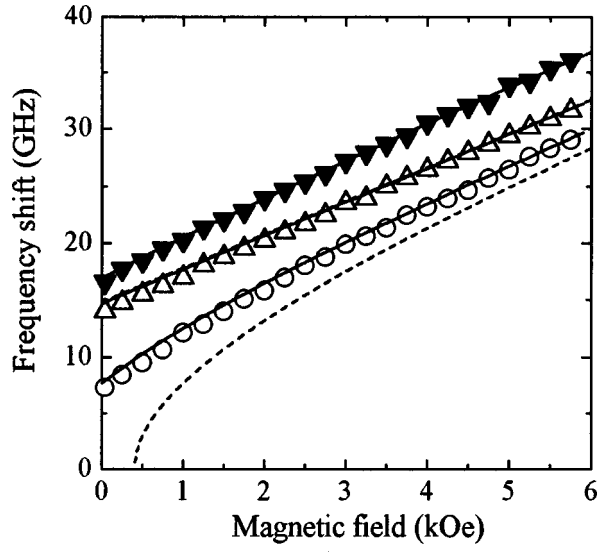

FIG. 5. The same as Fig. 4 in (110) $Ni_{81}Fe_{19}$(300 Å)/Cu(25Å)/$Ni_{81}Fe_{19}$(300 Å), with the field applied along an easy magnetization axis ($\phi=90°$).

sured in the isotropic (100) sample with $d=200$ Å, shown in Fig. 4, and in the 300 Å (110) sample with H_0 along the easy axis shown in Fig. 5.

In order to demonstrate the importance of the dipolar interaction in the dynamics of the system we show in Fig. 4 the comparison of the data for the (100) Py(200 Å)/Cu(25 Å)/Py(200 Å) sample with three theoretical results. The dotted line represents a fit with the calculation of Grünberg[3] which treats the dipolar coupling exactly in the limit of vanishing exchange and anisotropy interactions. The parameters used for the fit are the nominal magnetic and spacer layers thicknesses, saturation magnetization $4\pi M=9.0$ kG, spectroscopic factor $g=2.15$ and spin-wave wave number $q=1.73\times10^5$ cm^{-1}. The solid lines represent the results of our calculation, Eq. (48), using the same previous parameters and vanishing exchange and anisotropy fields. The volume mode curve is obtained by properly including anisotropy to the usual spin-wave expression, using an intralayer exchange stiffness $D=1.9\times10^{-9}$ Oe cm^2. We conclude that for this magnetic layer thickness and wave number, corresponding to a product $qd=0.34<1$, our calculation treats the dipolar interaction quite well based on its agreement with the data and Grünberg's results. The same is not true for the calculation of Cochran *et al.*,[12] represented in Fig. 4 by the dashed lines. While the two calculations give the same result for the acoustic mode, which does not depend on the coupling between the two magnetic layers, they depart from each other considerably for the optic mode, which does depend on the coupling.

Note that the result obtained with the approximations in Ref. 12 becomes worse as the optic mode frequency decreases. Again this results from the crude approximations made in the dipolar field expansions, since the lower the frequency the more important the dipolar energy is as compared to the Zeeman contribution. This is also seen in the comparison between the data for the anisotropic 200 Å sample on MgO (110) in Fig. 3 and the calculated dispersion relations. Our result (solid line) provides a good fit to the data for all modes using the parameters $4\pi M=9.0$ kG, $H_{au}=0.55$ kOe, $g=2.1$, and $D=2\times10^{-9}$ Oe cm^2. However, the approach in Ref. 12 (dashed line) with the same parameters departs from the data for the optic mode, especially in the low frequency region. Note that we do not show in Fig. 3 the dispersion calculated with Grünberg's theory because it does not include the anisotropy energy. The departure between the theoretical approximations in Ref. 12 and data becomes larger for thicker magnetic layers. This is seen in Fig. 5 which shows the data for the 300 Å sample on MgO (110) and the dispersion relations calculated with our result (solid line) and with the approximations in Ref. 12 (dashed lines).

Since the dipolar interaction becomes more important with increasing qd, it is interesting to compare the three theoretical results with the spin-wave dispersion as a function of the wave number. This is shown in Fig. 6 for the (100) Py(300 Å)/Cu(25 Å)/Py(300 Å) trilayer in a constant in-plane field $H_0=1.0$ kOe. The wave number is varied by changing the scattering incidence angle in the range $15°<\alpha<60°$. Again, the dotted, solid, and dashed lines represent, respectively, the calculations of Ref. 3, ours and the one in Ref. 12. As clearly seen, all calculations give the same result for the vanishing wave number because the dipolar and the intralayer exchange interactions vanish in this limit. However, as q increases, the three calculations depart from each other. While our calculation agrees quite well with experiments, the results of Ref. 3 depart slightly from the data because it does not take into account the intralayer exchange. On the other hand, the results of Ref. 12 depart considerably from the data for high q values because the approximations made in the dipolar field calculation are not satisfactory in this range. Note, however, that since the important parameter in the dipolar field expansion is the product qd, the calculation in Ref. 12 would be quite satisfactory in the high q range for film thicknesses $d<50$ Å.

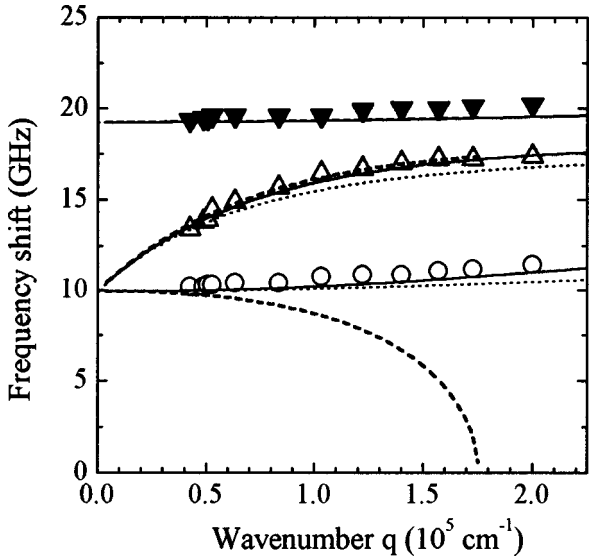

FIG. 6. BLS frequency shift vs magnon wave number q in (100) $Ni_{81}Fe_{19}$(300 Å)/Cu(25 Å)/$Ni_{81}Fe_{19}$(300 Å). Lines and symbols are as in Fig. 4.

VI. BILINEAR AND BIQUADRATIC EXCHANGE IN (100) Fe/Cr/Fe TRILAYERS

Having established that the spin wave calculation presented in Sec. III treats accurately the dipolar interaction between two magnetic layers, we now apply that calculation to investigate the exchange coupling in several sputtered (100) Fe/Cr/Fe trilayers. Actually, for thicknesses of the ferromagnetic layer smaller than about 100 Å, as is the case of the Fe/Cr/Fe samples studied here, a higher-order approximation to the dipolar field is shown to play an important role. As will be shown, it is also essential to include the effect of the biquadratic exchange interaction.

Fe/Cr films can be prepared in single-crystal form by several techniques, such as molecular beam epitaxy, electron beam deposition, and sputtering.[1,16] Since the nature of the coupling between the magnetic layers depends on the chemical composition and on the details of the microstructure, Fe/Cr systems grown by different methods have become a prototype for studies of coupling in magnetic multilayers. In particular, the peculiar biquadratic coupling has been ob-

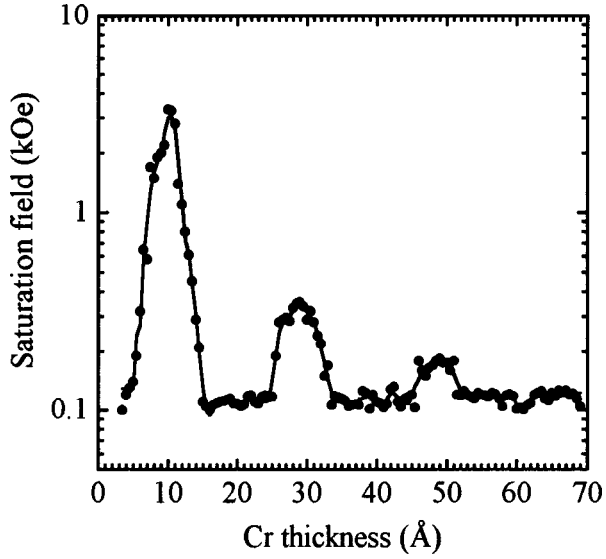

FIG. 7. Saturation field measured with MOKE magnetometry in a Fe/Cr/Fe wedge as a function of the Cr thickness (Ref. 26). The solid line is a guide to the eyes.

served in Fe/Cr/Fe trilayers by several authors.[24–28] Here we show that the static and dynamic properties of this system are very sensitive to the biquadratic interaction. This fact is used to measure both the bilinear and biquadratic couplings as a function of the spacer layer thickness in sputtered (100) Fe(40 Å)/Cr(s)/Fe(40 Å).

In order to determine the overall behavior of the coupling as a function of spacer thickness we have done easy axis MOKE magnetometry measurements in a wedged trilayer structure. Figure 7 shows a plot of the saturation field as a function of the Cr layer thickness. The saturation field is defined arbitrarily as the field at which the moment reaches 75% of the saturation value. Note that the coupling reaches the first antiferromagnetic (AF) maximum at about $s=10$ Å, crosses to ferromagnetic at $s=15$ Å, crosses back to AF at $s=25$ Å, and reaches the second AF peak at $s=29$ Å. Since this behavior is primarily determined by the bilinear exchange parameter J_1, it is of interest to find out how the biquadratic exchange constant J_2 varies as J_1 changes with s. In order to extract accurate values for J_1 and J_2 we have studied three trilayer samples having uniform Cr spacers with thickness $s=11$, 15, and 25 Å.

A. MOKE and FMR in (100) Fe(40 Å)/Cr(11 Å)/Fe(40 Å)

Consider first, the (100) Fe/Cr/Fe sample with Cr thickness $s=11$ Å, a value close to the first AF maximum. The initial characterization is made with MOKE magnetometry. Figure 8(a) shows data (open circles) measured with the field along the easy [001] axis. The solid line represents a theoretical fit with the calculation described in Sec. II, using the following parameters: $4\pi M=19.5$ kG, $H_{ac}=2K_1/M=0.57$ kOe, $H_u=H_s=0$, $H_{ex1}=J_1/d_1M=-0.89$ kOe ($J_1=-0.55$ erg/cm^{-2}), $H_{ex2}=J_2/d_1M=0.07$ kOe ($J_2=0.044$ erg/cm^2, $J_2/J_1=-0.08$). The corresponding equilibrium angles θ_1 and θ_2 are shown in Fig. 8(b). The arrows represent the evolution of the spacial configuration of the magnetizations in the Fe films towards saturation. At low

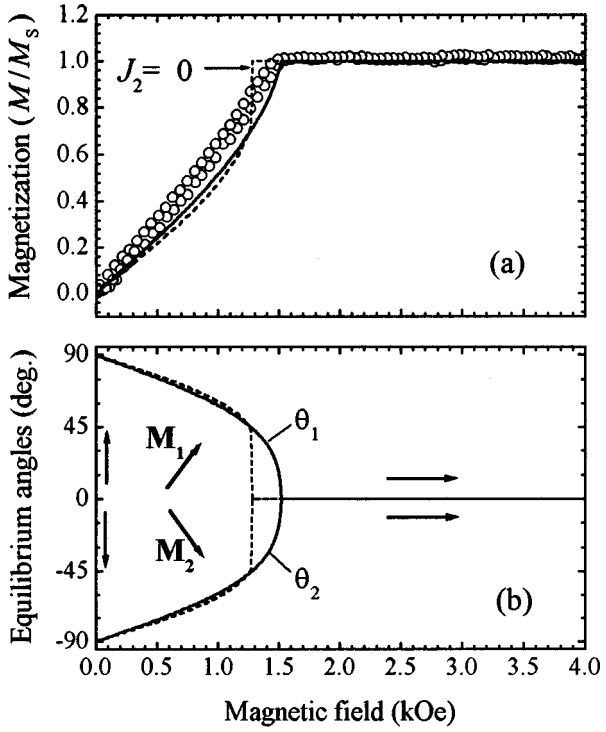

FIG. 8. Normalized magnetization vs external field H_0 applied along [001] ($\theta_H=0$), in (100) Fe(40 Å)/Cr(11 Å)/Fe(40 Å). Open circles are MOKE data. Lines are calculated. (b) Calculated equilibrium magnetization angles θ_1 and θ_2 vs H_0.

fields $\mathbf{M}_1$ and $\mathbf{M}_2$ are aligned nearly opposite to each other and perpendicular to $\mathbf{H}_0$, in a canted-spin configuration. As the field increases and the Zeeman energy becomes more important, the magnetizations gradually rotate towards the field. Saturation occurs at fields larger than a critical value H_{SAT}. For identical magnetic films, this value can be obtained analytically from the condition of vanishing derivative of Eq. (9) with respect to $\theta=\theta_1=-\theta_2$, and is given by

$$H_{SAT}=2|H_{ex1}|+4H_{ex2}\mp H_{ac}, \tag{57}$$

where the sign $-$ ($+$) occurs when the field is applied along an easy (hard) magnetization axis. The parameters above lead to a critical field $H_{SAT}=1.49$ kOe. Note that the presence of a small biquadratic exchange does not change the nature of the equilibrium phase [dashed line in Fig. 8(a)]. A positive J_2 changes the curvature of the magnetization curve near the critical field and slightly increases the value of H_{SAT}. Furthermore, notice that in the case of Fig. 8 H_{SAT} is no longer given by Eq. (57) when $J_2=0$, since saturation is reached through a first-order transition.

A remarkably distinct phase diagram occurs when the field $\mathbf{H}_0$ is applied along the hard [101] axis, i.e., $\theta_H=45°$. Figure 9 shows the equilibrium angles and the magnetization versus field for this case, where three distinct phases are observed. At fields below a certain critical value of 0.5 kOe, the magnetizations remain close to an antiferromagnetic (AF) alignment along the [001] axis. At this field there is a sudden transition to a spin–flop (SF) state. As the field increases above this value, the spins rotate towards the field and only at 2.63 kOe the system attains saturation. Again,

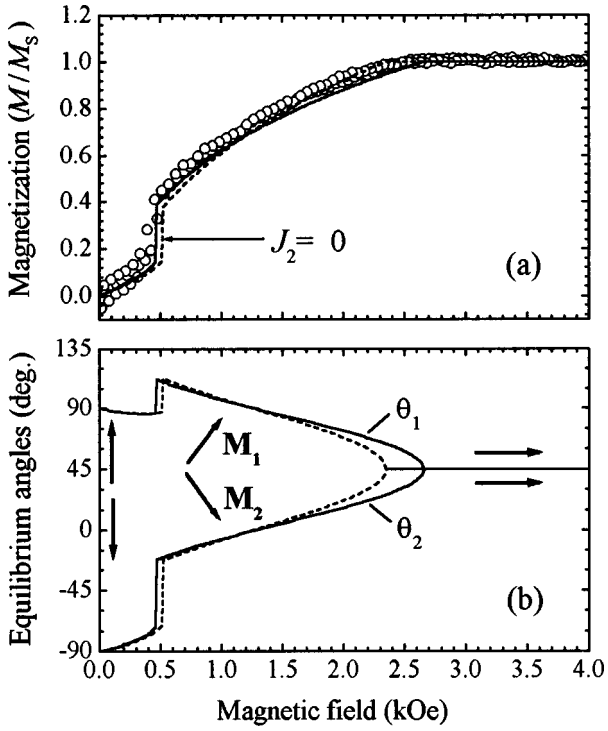

FIG. 9. Same as Fig. 8, with H_0 applied along [101] ($\theta_H = 45°$).

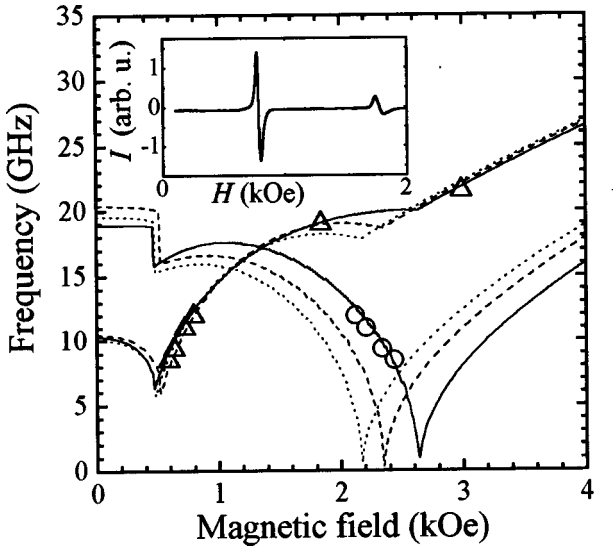

FIG. 10. Symbols: Variable-frequency FMR measurements in (100) Fe(40 Å)/Cr(11 Å)/Fe(40 Å) with the external field H_0 applied along [101] ($\theta_H = 45°$). Solid, dashed, and dotted lines are results of calculations. Inset: FMR spectrum at 9.5 GHz and $\theta_H = 30°$.

note that the existence of a small positive J_2 does not change the nature of the phases, it only varies the curvature of M vs H_0 and changes the values of the critical fields.

There are three independent components in the critical field given in Eq. (57). It should be possible to determine the three field parameters from the simultaneous fittings of the two magnetization curves in Figs. 8(a) and 9(a). However, we find that the parameters that give the best least-square fit to the [101] data [solid line in Fig. 9(a)] produce a slight departure between theory and data for the [001] direction [solid line in Fig. 8(a)]. The uncertainty in the value of H_{ex2} is considerable when its magnitude is much smaller than H_{ex1}.

Better accuracy in the determination of all magnetic parameters is achieved with BLS and FMR techniques. In order to obtain reliable fits between theory and experiment it is necessary to measure the variation of some spin-wave quantity as a function of a convenient parameter. In the case of FMR one can measure the field for resonance at constant microwave frequency as a function of the azimuthal in-plane angle θ_H as the sample is rotated in its plane.[1,16,29,30] Alternatively, it is possible to employ several microwave cavities to vary the frequency discretely and obtain the $q=0$ spin-wave dispersion relations.[13] However, in both cases it is necessary to observe both acoustic and optic modes in order to extract accurate values for the exchange coupling constants.

Figure 10 shows the dispersion relations for the $q=0$ modes with the magnetic field H_0 applied along the hard [101] axis ($\theta_H = 45°$). The symbols represent the data and the lines are theoretical results obtained with Eq. (52) with the same parameters used to fit the MOKE data in Fig. 9(a). As the equilibrium state, the dispersion relations are characterized by three distinct phases: AF for $0 < H_0 < 0.5$ kOe; spin–flop (SF) for 0.5 kOe$< H_0 <$2.63 kOe; and saturated or FM for $H_0 > 2.63$ kOe. The inset shows a typical spectrum at 9.5 GHz and $\theta_H = 30°$, where one acoustic mode and one optic mode resonance are seen. Note that the optic mode resonance expected for $H_0 > H_{SAT}$ is not observed because its intensity in the FM phase is theoretically zero. As seen in Fig. 10, the behavior of the frequency versus field for both acoustic and optic modes is different in each phase. This results from the fact that the frequencies of the magnetic excitations depend directly on the configuration of the magnetizations in both films, as shown by Eqs. (53)–(56). As in Fig. 9(a) the dashed line is obtained with $H_{ex2}=0$, keeping the same values for the other parameters. As expected, this produces a large departure of the optic mode line from the data because the critical field for the SF–FM transition is very sensitive to the value of H_{ex2}. One may ask what happens if we keep $H_{ex2}=0$ and vary the other parameters to obtain a least-square fit to the data. The result is shown by the dotted line in Fig. 10, obtained with $4\pi M = 19.5$ kOe, $H_{ac}=0.53$ kOe, $H_{ex1}=-0.82$ kOe, and $g=2.1$. This shows that although H_{ex2} is small, it is not possible to fit the data to the theory without inclusion of the biquadratic exchange energy in the calculation. The estimated maximum error in the values of the parameters extracted from the fit is 3% based on the visual departure of the curves from the least-square fit.

Another way to obtain data with the FMR technique is by keeping the frequency fixed and measuring the resonance field for the acoustic and optic modes as the sample is rotated about its normal, maintaining the field in the plane. The measured field variations with angle exhibits fourfold symmetry due to the cubic anisotropy of Fe (100). Figure 11 shows the data obtained with a frequency of 9.5 GHz in one quadrant together with theoretical lines calculated with Eq. (52). The solid line is the least-square fit obtained with parameters almost identical to the previous values, namely: $4\pi M = 19.5$ kOe, $H_{ac}=0.57$ kOe, $H_{ex1}=-0.89$ kOe, H_{ex2}

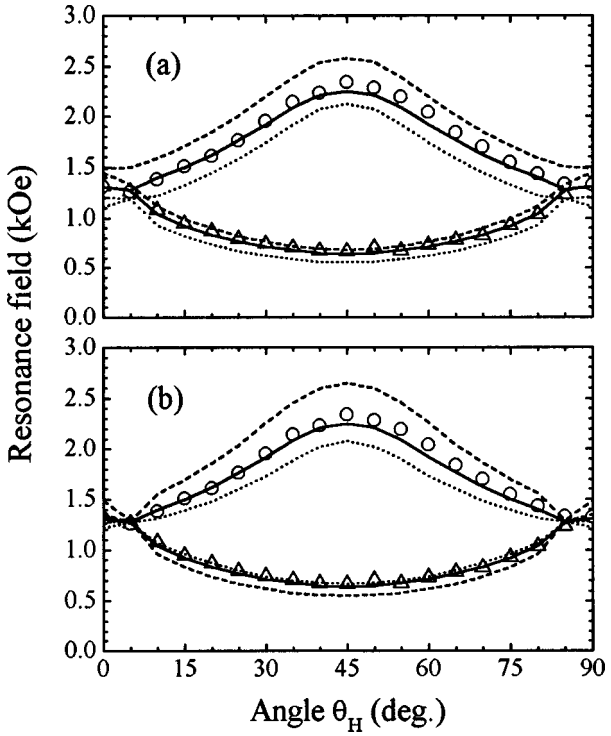

FIG. 11. Resonance field vs in-plane field angle θ_H in (100) Fe(40 Å)/Cr(11 Å)/Fe(40 Å). Open circles are for the measured FMR optic mode and the open triangles for the acoustic mode. The solid lines are the best theoretical fits obtained. The solid lines in (a) and (b) were obtained with the exchange field parameters $(H_{ex1}, H_{ex2}) = (-0.89\ \text{kOe},\ 0.07\ \text{kOe})$. (a) the dashed (dotted) line was obtained with $H_{ex2} = 0.07$ kOe and $H_{ex1} = -1.0$ kOe $(-0.80$ kOe). (b) the dashed (dotted) line was obtained with $H_{ex1} = -0.89$ kOe and $H_{ex2} = 0.14$ kOe (0 kOe).

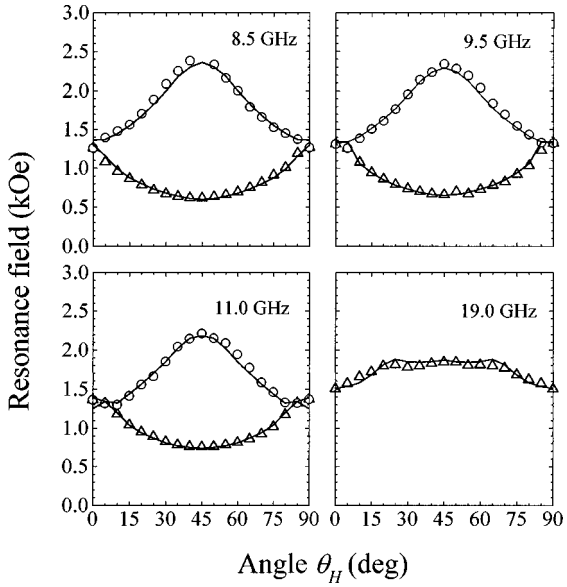

FIG. 12. Comparison between FMR data at several frequencies and theory with the same parameters used to obtain the solid lines in Fig. 11.

$= 0.07$ kOe, and $g = 2.1$. As can be seen by the dashed and dotted lines in Figs. 11(a) and 11(b), the resonance field increases with increasing $|H_{ex1}|$ and H_{ex2}. In order to show the consistency of the set of parameters extracted from this fit, we show in Fig. 12 the comparison between data taken at four other frequencies with the theoretical prediction obtained with the same parameter values. Even the curious triple peaked shape of the data at 19 GHz is very well reproduced. The dispersion relations obtained with these parameters for $q \neq 0$ are also in excellent agreement with the BLS data for this sample.

B. (100) Fe(40 Å)/Cr(15 Å)/Fe(40 Å)

When the sample with Cr thickness $s = 15$ Å was first investigated it was expected to have a small antiferromagnetic coupling and correspondingly small critical fields for all magnetic phase transitions. However, besides the expected low critical fields, the data furnished by the various techniques displayed surprisingly sudden jump as the field varied. This was soon found to be a result of abrupt phase transitions in the magnetic state produced by the relatively large biquadratic exchange.[26,27] Figure 13(a) shows MOKE measurements in the field range $0 < H_0 < 0.4$ kOe, applied along the easy axis. The circles in the inset are MR data, obtained with a standard four-probe technique. Both data without the coercive field are very well fitted by the theoretical lines shown in Fig. 13(a), obtained with Eqs. (10) and (11) with the parameters: $4\pi M = 19.0$ kG, $H_{ac} = 0.55$ kOe, $H_{ex1} = -0.15$ kOe, $H_{ex2} = 0.05$ kOe. The exchange fields correspond to the parameters $J_1 = -0.09$ erg/cm^2 and $J_2 = 0.03$ erg/cm^2. This relatively large biquadratic coupling is responsible for the two first-order phase transitions that produce the jumps in the data. As shown in Fig. 13(b), at $H_0 \simeq 0.1$ kOe the alignment changes from AF to nearly 90°; at $H_0 \simeq 0.22$ kOe it changes from 90° to FM alignment.

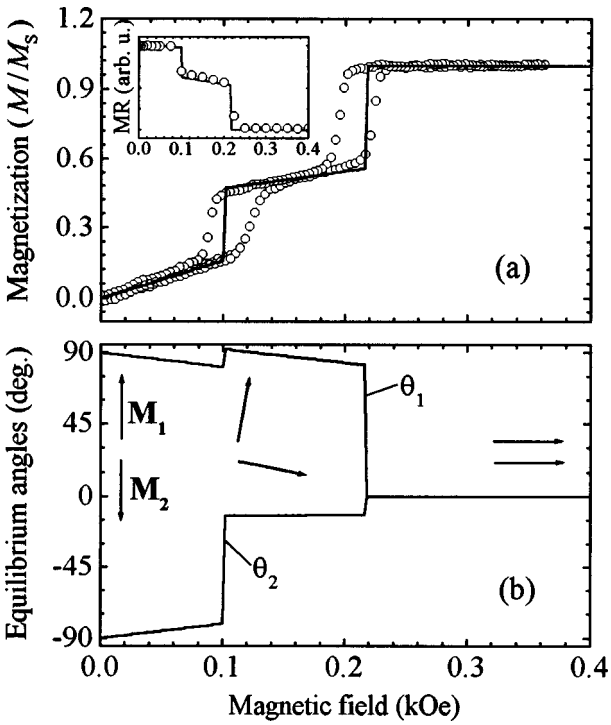

FIG. 13. (a) Open circles: easy-axis MOKE data in (100) Fe(40 Å)/Cr(15 Å)/Fe(40 Å). Inset: open circles: corresponding magnetoresistance data. Solid lines are fits with Eqs. (11) and (10), respectively. (b) Calculated equilibrium magnetization angles vs external field H_0.

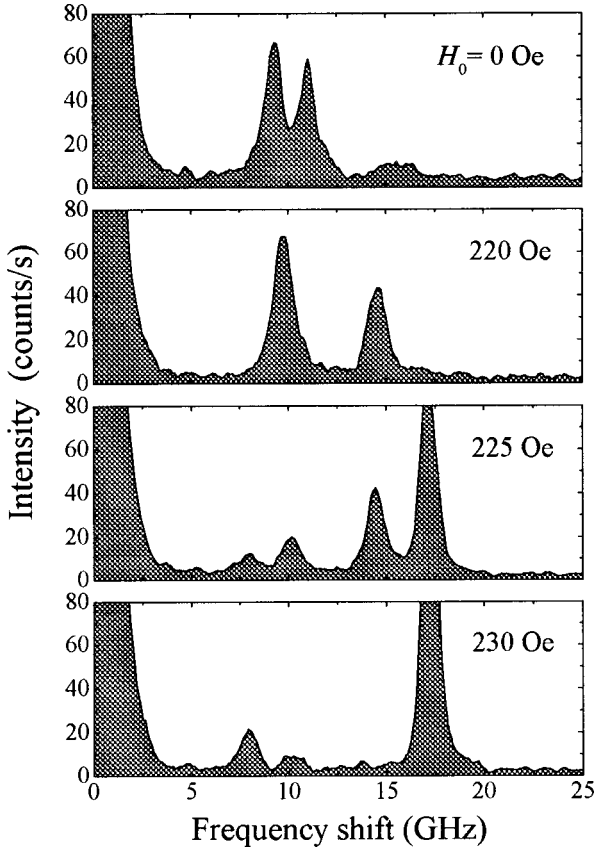

FIG. 14. Measured BLS spectra in (100) Fe(40 Å)/Cr(15 Å)/Fe(40 Å) for four different values of the applied field, corresponding to different regions of the magnetization curve shown in Fig. 13. (a) AF phase at $H_0=0$; (b) near 90° phase at 0.220 kOe; (c) mixed-domain state at 0.225 kOe; (d) saturated phase at 0.230 kOe.

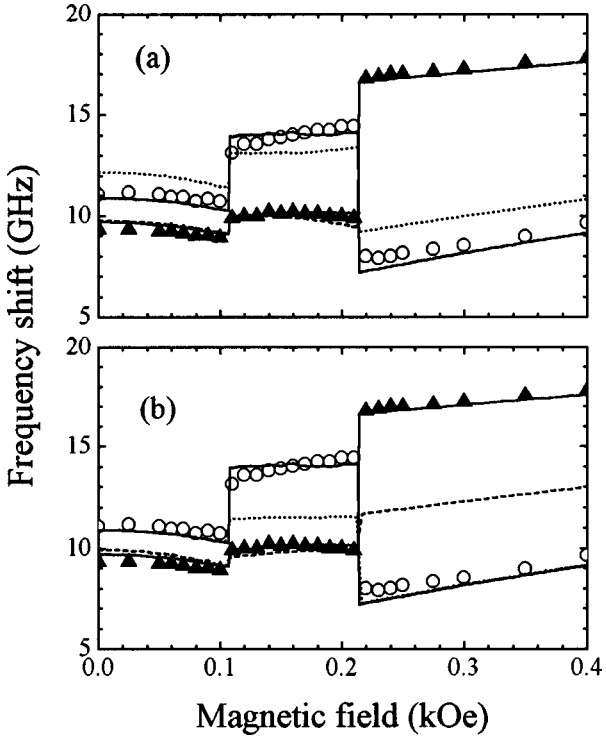

FIG. 15. Magnon frequencies for $q=1.22\times10^5$ cm^{-1} vs external field H_0, applied along an easy magnetization axis in (100) Fe(40 Å)/Cr(15 Å)/Fe(40 Å). Symbols are BLS data: solid triangles for the acoustic mode and open circles for the optic mode. Solid lines are results of calculations with Eq. (52) with the same parameters as in Fig. 13. The dotted lines in (a) were obtained with $H_{ex2}=0$. The dotted lines in (b) were obtained without the volume contribution to the rf dipolar field.

Steps due to first-order phase transitions are also observed in the spin-wave frequency versus field data obtained with BLS. Figure 14 shows spectra obtained at several fields applied along the [001] axis in the backscattering geometry with an incidence angle of 30°, corresponding to a magnon wave number $q=1.22\times10^5$ cm^{-1}. The spectra were measured with laser power of 100 mW and 2000 interferometer scans. Only the anti-Stokes peaks are shown in Fig. 14. In the AF phase, shown in Fig. 14(a) at zero field, the two magnon modes are separated in frequency by about 2 GHz, the optic mode having higher frequency than the acoustic one. When the field is increased above 0.1 kOe the system acquires the near 90° alignment and the separation between the acoustic and optic modes suddenly increases. The two peaks at $H_0=0.220$ kOe [Fig. 14(b)] are 5 GHz apart. At $H_0=0.230$ kOe the system reaches the FM state, and the acoustic mode frequency becomes higher than the optic mode frequency. It is interesting to observe that at $H_0=0.225$ kOe [Fig. 14(c)], the peaks corresponding to the 90° and FM phases are simultaneously present, probably due to the formation of a domains state.

The overall behavior of the frequency shift as a function of the applied field is shown in Fig. 15(a). Open circles (solid triangles) represent the measured optic-mode (acoustic-mode) frequencies. The solid lines are the spin-wave frequencies calculated from Eq. (48), with the same set of realistic parameters used in Fig. 13. Again, there is excellent agreement between theory and data. Note that the inversion of the relative positions of the acoustic and optic modes at the second transition ($H_0\sim0.22$ kOe) is predicted by theory. The dotted lines in Fig. 15(a) represent the frequencies calculated without the contribution of the biquadratic exchange field in Eq. (48). Actually, H_{ex2} has been kept in the energy expression (9), to preserve the correct ground states. The most pronounced effect of the biquadratic coupling in this case is to shift the frequency of the optic mode, downwards in the AF and FM phases and upwards in the 90° central region. In order to further investigate the effect of the dipolar coupling in the dynamics, we show in Fig. 15(b) by dotted lines the frequencies calculated with the same parameters, but neglect the volume contribution to the dipolar field. The poor fit thus obtained is an indication of the important role played by the dipolar interaction, even in these thinner films. We finally mention that the calculated resonance field versus in-plane azimuth angle, with the same parameters used to obtain the solid lines in Fig. 15, is also in excellent agreement with FMR data.[26]

C. (100) Fe(40 Å)/Cr(25 Å)/Fe(40 Å)

The last sample studied has a Cr thickness $s=25$ Å near the second AF–FM coupling transition. Figure 16 shows the calculated equilibrium angles θ_1 and θ_2 (upper panel), and BLS data (lower panel), obtained with the field applied along

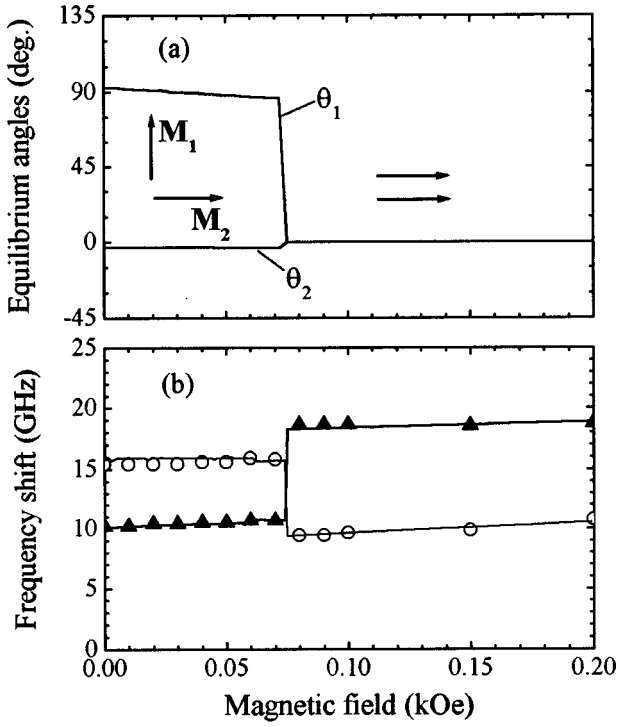

FIG. 16. (a) Calculated easy-axis equilibrium magnetization angles and (b) corresponding BLS data (symbols) and fit (solid lines) in (100) Fe(40 Å)/Cr(25 Å)/Fe(40 Å).

[001] in the range $0<H_0<0.2$ kOe. The solid lines are theoretical fits with Eqs. (9) and (48) with parameters: $4\pi M=20.5$ kOe, $H_{ac}=0.55$ kOe, $H_{ex1}=-0.036$ kOe, $H_{ex2}=0.036$ kOe, $g=2.1$. The exchange fields correspond to the parameters $J_1=-0.024$ erg/cm^2 and $J_2=0.024$ erg/cm^2, so that $J_2/|J_1|=1.0$. We note that the unity $J_2/|J_1|$ ratio prevents the system to acquire the AF state. In this case the system has only two phases, near-90° and FM, separated by a first-order transition, which is clearly manifested in the MOKE and BLS data.

VII. SUMMARY

A theory for treating low wave number spin waves in exchange and dipolar coupled ferromagnetic films in trilayer structures was presented in this article. In addition to bilinear and biquadratic exchange, the theory takes full account of surface, in-plane uniaxial, and cubic anisotropy interactions. Analytical expressions are given for $q\neq 0$ modes, as observed in BLS experiments, and $q=0$ modes detected by FMR techniques. The validity of the treatment of the dipolar interaction was successfully demonstrated in moderately thick trilayers of NiFe/Cu/NiFe. The theoretical results were used to interpret data obtained in sputtered (100) Fe(40 Å)/Cr(s)/Fe(40 Å) with $s=11$, 15, and 25 Å by magnetoresistance measurements, MOKE, BLS, and FMR. The parameter sets determined by independent fittings to the data obtained through the various techniques are all consistent. As expected, we find that the bilinear exchange parameter varies strongly with the investigated Cr layer thickness, namely, $J_1=-0.55$, -0.09, and -0.024 erg/cm^2 for $s=11$, 15 and 25 Å, respectively, corresponding to a field $H_{ex1}=-0.89$, -0.15, and -0.036 kOe. On the other hand, the biquadratic exchange parameter does not vary much; $J_2=0.044$, 0.030, 0.024 erg/cm^2, or $H_{ex2}=0.070$, 0.050, and 0.036 kOe for $s=11$, 15, and 25 Å, respectively. The consistent experimental support to our model calculations, provided by the samples and techniques discussed in this paper, has led us to exploit its richness in further studies. In particular, interesting phase diagrams for the equilibrium configuration of the magnetizations can be predicted. Results in this regard will be published elsewhere.[31]

ACKNOWLEDGMENTS

The authors thank K. P. Roche for technical support, X. Bian for helping in some experiments, and P. Kabos for stimulating discussions. The work at UFPE has been supported by CNPq, CAPES, PADCT, FINEP, and FACEPE (Brazilian agencies). The work at IBM was partially supported by the Office of Naval Research.

[1] See, for example, P. Grünberg, in *Light Scattering in Solids V*, edited by M. Cardona and G. Güntherodt, Topics in Applied Physics Vol. 66 (Springer, Berlin, 1989), Chap. 8; M. H. Grimsditch, *ibid.*, Chap. 7; B. Heinrich and J. F. Cochran, in *Ultrathin Magnetic Structures*, edited by B. Heinrich and J. A. C. Bland (Springer, Berlin, 1994), Vol. II, Chap. 3; J. R. Dutcher, in *Linear and Nonlinear Spin Waves in Magnetic Films and Superlattices*, edited by M. G. Cottam (World Scientific, Singapore, 1994), Chap. 6.
[2] R. W. Damon and J. R. Eshbach, J. Phys. Chem. Solids **19**, 308 (1961).
[3] P. Grünberg, J. Appl. Phys. **51**, 4338 (1980); *ibid.* **52**, 6824 (1981).
[4] R. E. Camley, T. S. Rahman, and D. L. Mills, Phys. Rev. B **23**, 1226 (1981).
[5] P. Grünberg, R. Schreiber, Y. Pang, M. B. Brodsky, and H. Sowers, Phys. Rev. Lett. **57**, 2442 (1986).
[6] F. Hoffman, A. Stankoff, and H. Pascard, J. Appl. Phys. **41**, 1022 (1970); F. Hoffman, Phys. Status Solidi **41**, 807 (1970).
[7] J. Barnas and P. Grünberg, J. Magn. Magn. Mater. **126**, 380 (1993).
[8] J. Slonczewski, Phys. Rev. Lett. **67**, 3172 (1991); J. Magn. Magn. Mater. **150**, 13 (1995).
[9] B. Hillebrands, Phys. Rev. B **41**, 530 (1990).
[10] M. Vohl, J. Barnas, and P. Grünberg, Phys. Rev. B **39**, 12 003 (1989).
[11] B. Heinrich, S. T. Purcell, J. R. Dutcher, K. B. Urquhart, J. F. Cochran, and A. S. Arrott, Phys. Rev. B **38**, 12 879 (1988).
[12] J. F. Cochran, J. Rudd, W. B. Muir, B. Heinrich, and Z. Celinski, Phys. Rev. B **42**, 508 (1990).
[13] J. J. Krebs, P. Lubitz, A. Chaiken, and G. A. Prinz, Phys. Rev. Lett. **63**, 1645 (1989); J. Appl. Phys. **67**, 5920 (1990).
[14] A. Layadi and J. O. Artman, J. Magn. Magn. Mater. **92**, 143 (1990).
[15] P. E. Wigen and Z. Zhang, Braz. J. Phys. **22**, 267 (1992).
[16] B. Heinrich and J. F. Cochran, Adv. Phys. **42**, 523 (1993).
[17] R. L. Stamps, Phys. Rev. B **49**, 339 (1994).
[18] Z. Zhang, L. Zhou, P. E. Wigen, and K. Ounadjela, Phys. Rev. B **50**, 6094 (1994).
[19] Y. Roussigné, F. Ganot, C. Dugautier, P. Moch, and D. Renard, Phys. Rev. B **52**, 350 (1995).
[20] P. Kabos, C. E. Patton, M. O. Dima, and D. B. Church, J. Appl. Phys. **75**, 3553 (1994).
[21] E. E. Fullerton, M. J. Conover, J. E. Mattson, C. H. Sowers, and S. D. Bader, Phys. Rev. B **48**, 15 755 (1993).
[22] X. Bian, H. T. Hardner, and S. S. P. Parkin, J. Appl. Phys. **79**, 4980 (1996).
[23] M. A. Lucena, F. M. de Aguiar, S. M. Rezende, A. Azevedo, C. Chesman, and S. S. P. Parkin, J. Appl. Phys. **81**, 4770 (1997).
[24] M. Ruhrig, R. Schafer, A. Hubert, R. Mosler, J. A. Wolf, S. Demokritov, and P. Grünberg, Phys. Status Solidi A **125**, 635 (1991).
[25] J. Unguris, R. J. Celotta, and D. T. Pierce, Phys. Rev. Lett. **67**, 140 (1991).
[26] A. Azevedo, C. Chesman, S. M. Rezende, F. M. de Aguiar, X. Bian, and S. S. P. Parkin, Phys. Rev. Lett. **76**, 4837 (1996).

[27] C. Chesman, A. Azevedo, S. M. Rezende, F. M. de Aguiar, X. Bian, and S. S. P. Parkin, J. Appl. Phys. **81**, 3791 (1997).
[28] M. Grimsditch, S. Kumar, and E. E. Fullerton, Phys. Rev. B **54**, 3385 (1996).
[29] B. Heinrich, J. F. Cochran, M. Kowalewski, J. Kirschner, Z. Celinski, A. S. Arrot, and K. Myrtle, Phys. Rev. B **44**, 9348 (1991).
[30] S. M. Rezende, F. M. de Aguiar, A. Azevedo, M. A. Lucena, C. Chesman, P. Kabos, and C. E. Patton, Phys. Rev. B **55**, 8071 (1997).
[31] C. Chesman, M. A. Lucena, A. Azevedo, F. M. de Aguiar, S. M. Rezende, and S. S. P. Parkin, Phys. Rev. B (to be published).